JGR Space Physics

RESEARCH ARTICLE
10.1029/2025JA034259

Velocity and Magnetic Fluctuations Across Machine Learning Defined Regions of the Magnetotail Plasma Sheet

Jiye Wang[1,2], Xuan Liu[1], Fanzhuo Dai[2], Wence Jiang[2], Yang Wang[3], Andi Liu[3], Hui Li[2], Lingqian Zhang[2], Chi Wang[2], Xinhua Wei[2], James L. Burch[4], Wolfgang Baumjohann[5], Tieyan Wang[6], Rui Zheng[1], Hongxia Qing[1], and Chuwei Lyu[1]

[1]Information Engineering College, MinZu University of China, Beijing, China, [2]State Key Laboratory of Solar Activity and Space Weather, National Space Science Center, Chinese Academy of Sciences, Beijing, China, [3]College of Information and Communication Engineering, Beijing Information Science and Technology University, Beijing, China, [4]Southwest Research Institute San Antonio, San Antonio, TX, USA, [5]Space Research Institute, Austrian Academy of Sciences, Graz, Austria, [6]Department of Geophysics, School of Earth Sciences, Yunnan University, Kunming, China

Abstract We present a comprehensive analysis of magnetic and velocity fluctuations in Earth's magnetotail plasma sheet based on observations from the Magnetospheric Multiscale (MMS) mission during its 2017 magnetotail campaign. Utilizing a novel Hybrid Filter–Decision Tree Model (HFDTM), we systematically classify the plasma sheet ($X < -10$ R_E in Geocentric Solar Ecliptic coordinates) into four key regions: the current sheet (CS), central plasma sheet (CPS), plasma sheet boundary layer (PSBL), and tail lobe. Within each region, we examine fluctuation dynamics across three critical flow regimes, including stagnant ($V < 50$ km s^{-1}), sub-Alfvénic (50 km s^{-1} $\leq V < V_A$), and super-Alfvénic ($V \geq V_A$). Our key findings reveal: (a) Anisotropy Transition: Magnetic field anisotropy reverses with increasing flow speed, shifting from near-isotropic values ($\Delta B_{\parallel}/\Delta B_{\perp} \approx 1.1$) under stagnant conditions to strongly perpendicular-dominated distributions (~0.4) in the super-Alfvénic regime; (b) Multimodal Heating: Multi-peak structures in the thermal energy (E_T) spectrum, along with the co-evolution of thermal (H_T) and kinetic (H_V) enstrophy from the CS to the PSBL, reveal a dual-pathway heating mechanism involving both kinetic and magnetic energy transfer; and (c) Correlation Structure: Across all regions and regimes, weak-to-moderate velocity–magnetic field correlations dominate, with enhanced $V_{\parallel}$-$B_{\parallel}$ correlations under super-Alfvénic flows. Collectively, these results identify the plasma sheet as a distinct turbulent regime, governed by localized energization mechanisms (e.g., reconnection, substorm dipolarization, and flow braking), marking a departure from the Alfvénic turbulence paradigm observed in the solar wind.

Plain Language Summary Earth's magnetotail, the stretched region behind the planet shaped by the solar wind, stores and releases energy through dynamic processes such as magnetic reconnection and substorms. In this study, we use data from NASA's Magnetospheric Multiscale (MMS) mission to investigate how energy moves through the magnetotail via magnetic and plasma (ion) fluctuations. Using a new machine learning model, we divide the magnetotail into four key regions and analyze how turbulence changes with different plasma flow speeds. We identify new turbulence behavior in Earth's plasma sheet. Specifically, we observed multiple peaks in thermal energy and coordinated patterns in thermal and kinetic enstrophy, indicating two simultaneous energy transfer pathways: magnetic and kinetic. These findings enhance our understanding of how energy is distributed and dissipated in space plasma and contribute to improving models of plasma sheet turbulence.

Key Points:

- A novel machine learning-based Hybrid Filter-Decision Tree Model (HFDTM) is developed for automated classification of magnetotail regions
- Wavelet analyses reveal multimodal heating, indicating dual pathways of kinetic and magnetic energy transfer
- Weak and moderate *V-B* correlations dominate across all regions and flows, suggesting enhanced intermittency in plasma sheet turbulence

Correspondence to:
H. Li and L. Zhang,
lihui@nssc.ac.cn;
lqzhang@nssc.ac.cn

Citation:
Wang, J., Liu, X., Dai, F., Jiang, W., Wang, Y., Liu, A., et al. (2025). Velocity and magnetic fluctuations across machine learning defined regions of the magnetotail plasma sheet. *Journal of Geophysical Research: Space Physics*, *130*, e2025JA034259. https://doi.org/10.1029/2025JA034259

Received 3 JUN 2025
Accepted 22 JUL 2025

Author Contributions:
Data curation: Xuan Liu, Hongxia Qing
Formal analysis: Fanzhuo Dai, Wence Jiang
Investigation: Rui Zheng, Chuwei Lyu
Methodology: Xinhua Wei, Tieyan Wang
Project administration: Jiye Wang, Chi Wang
Software: Yang Wang, Andi Liu
Writing – original draft: Lingqian Zhang
Writing – review & editing: Hui Li, James L. Burch, Wolfgang Baumjohann

1. Introduction

The solar wind, a collisionless high-conductivity plasma with a nearly frozen-in interplanetary magnetic field (IMF), serves as a natural laboratory for studying magnetohydrodynamic (MHD) turbulence (Bruno & Carbone, 2013). Expanding at super-Alfvénic speeds (~400–800 km/s), it forms a nonlinear system with free boundaries, where flux-freezing dominates across most scales. The IMF, shaped by solar rotation into Parker's spiral, defines the heliosphere's radial–azimuthal structure (Parker, 1958). Superimposed magnetic fluctuations comprise both wave-like and convective components (Bendt et al., 2024; Serianni et al., 2007; Tu & Marsch, 1993; Zhao et al., 2022), revealing a complex interplay between Alfvénic turbulence and coherent structures, key features of collisionless plasma dynamics (Verscharen et al., 2019).

In contrast, turbulence in the Earth's magnetotail plasma sheet arises from flux-tube interchange instabilities and current sheet (CS) dynamics. Its magnetic field configuration is well described by the Harris-type profile:

$$\mathbf{B} = B_x \tanh(z/l)\,\hat{\mathbf{x}} + B_n\,\hat{\mathbf{z}}, \tag{1}$$

where B_x is the lobe field, $B_n \ll B_X$ is the normal component, and l is the sheet half-thickness. This structure supports tearing mode instability (Coppi et al., 1966) and magnetic reconnection under arbitrary guide field (B_Y) conditions (Nakamura et al., 2006; Schindler & Birn, 1982). The small yet essential normal field component (B_n) breaks antiparallel symmetry, enabling cross-field instabilities linked to substorm onset (Lui et al., 1991).

Unlike the solar wind's persistent outward flow, the plasma sheet is a quasi-steady, pressure-balanced system coupled to the ionosphere via field-aligned currents (Baumjohann et al., 1990; Lockwood & Cowley, 2022; Milan et al., 2017). Energy enters through dayside reconnection and accumulates in the stretched CS as magnetic energy (Ma et al., 1995; Wang et al., 2014), which is subsequently released via two primary channels: (a) near-Earth substorms ($X \approx 8$–$12\ R_E$) (Baumjohann et al., 1999; Cheng, 2004; Kepko et al., 2015; Kozak et al., 2021; Petrukovich et al., 2000), and (b) mid-tail reconnection ($X \approx 20\ R_E$) (Baker et al., 1996; Palmroth et al., 2023; Sato & Hasegawa, 1982; Zhang et al., 2016). These processes mediate the transition from large-scale convection to localized energy dissipation in a turbulent plasma environment (Gonzalez & Mozer, 1974; Keiling, 2008; Strangeway & McFadden, 2008; Zimbardo et al., 2010). Previous studies have delineated three key regimes of plasma sheet turbulence:

1. *β-dependence*: Turbulence strength varies with plasma beta (β, the ratio of thermal pressure to magnetic pressure), peaking in the high-β central plasma sheet (CPS, $\beta \gtrsim 1$), weakening in the intermediate-β plasma sheet boundary layer (PSBL, $0.05 < \beta < 1$), and diminishing in the low-β lobe ($\beta < 0.05$) (Vörös et al., 2004, 2005).
2. *Reconnection-dependence*: Enhanced magnetic fluctuations are observed during bursty bulk flows (BBFs) (Ergun et al., 2018; Huang et al., 2012; Osman et al., 2015; Weygand et al., 2005).
3. *Substorm linkage*: Large-amplitude fluctuations during dipolarization events complement reconnection-driven dynamics (Neagu et al., 2002, 2005; El-Alaoui et al., 2013, 2021; Zhang, Wang, Dai, Ren, & Lui, 2022).

More recent observations from NASA's Magnetospheric Multiscale (MMS) mission have significantly advanced our understanding of BBF turbulence. The mission's multi-point measurements have uncovered several key features: (a) pronounced vorticity ($\boldsymbol{\omega} = \nabla \times \mathbf{V}$) within reconnection jets (Zhang et al., 2019), marking the first direct detection of organized rotational coherent structures; (b) scale-dependent perpendicular anisotropy, with kinetic-scale vorticity dominating over large-scale frozen-in flows (Zhang, Baumjohann, et al., 2020; Zhang, Wang, Dai, Baumjohann, et al., 2022); and (c) the emergence of eddy-dominated turbulence in field-aligned PSBL flows (Zhang et al., 2023), signaling a transition from wave-like to eddy-mediated dynamics (Borovsky & Bonnell, 2001; Borovsky et al., 1997). These findings establish BBF turbulence as a kinetic-scale phenomenon, where energy cascades from large-scale convection to localized dissipation via eddy-driven processes (Borovsky & Funsten, 2003; Oughton et al., 2015; Tian et al., 2010), thereby reframing our theoretical models of magnetotail turbulence (Weygand et al., 2006, 2009, 2011).

To systematically characterize turbulence across the plasma sheet, we applied a novel Hybrid Filter–Decision Tree Model (HFDTM) to data from the Magnetospheric Multiscale (MMS) mission during its 2016 magnetotail campaign. The structure of this paper is as follows: Section 2 describes the MMS data sets and preprocessing procedures. Section 3 outlines the architecture of the HFDTM and presents its validation. Section 4 investigates magnetic and plasma fluctuations as functions of plasma β. Section 5 presents statistical analyses, including velocity and magnetic field anisotropies, as well as wavelet-based energy and enstrophy metrics. Section 6 discusses the underlying turbulence characteristics by systematically analyzing velocity and magnetic field fluctuations in both parallel and perpendicular directions. Finally, Section 7 summarizes the key findings and implications of the study.

2. Method

2.1. Data Set Acquisition and Processing

This study utilizes low-resolution measurements from MMS mission (Burch et al., 2016), employing two core instruments: the Fluxgate Magnetometer (FGM) (Russell et al., 2016) for magnetic field observations and the Fast Plasma Investigation (FPI) (Pollock et al., 2016) for ion and electron plasma parameters. FGM provides magnetic field vectors at both 128 Hz (burst mode) and 8 Hz (survey mode), while FPI captures ion and electron distribution functions at 150 and 30 ms cadences, respectively.

To ensure temporal alignment between instruments and enhance computational efficiency, all data sets were uniformly downsampled to standardized time resolutions: 0.125 s (8 Hz) for magnetic field measurements and 4.5 s for plasma parameters. All quantities were analyzed in the Geocentric Solar Ecliptic (GSE) coordinate system. These harmonized cadences were selected to preserve key dynamical timescales characteristic of magnetotail processes, including dipolarization fronts (~10 s), substorm onsets (~60–200 s), and BBFs (~60–600 s). This approach enables reliable cross-comparisons between plasma and field variables while capturing the multiscale dynamics of the terrestrial plasma sheet.

2.2. Low-Pass Filter and Wavelet Analysis

To separate equilibrium fields from turbulent fluctuations, we applied a fourth-order Butterworth low-pass filter, implemented via MATLAB's butter function. The filter cutoff frequency was set to 1/600 Hz, corresponding to a 10-min period. This threshold effectively separates perturbations (capturing dynamic fluctuations driven by waves, reconnection, or turbulence) from background fields (representing slowly varying equilibrium structures). A shorter window, such as 5 min, may attenuate or distort key mesoscale structures—particularly the lower-frequency components of BBFs and flow braking signatures. These features are critical for understanding energy transport and turbulence in the magnetotail. On the other hand, a longer window (e.g., 15–20 min) tends to over-smooth the background magnetic and plasma fields, potentially masking important transitions between quasi-equilibrium states and dynamic fluctuation regimes. The 10-min window thus provides an optimal balance between noise suppression and preservation of physically meaningful transient structures.

The filtering procedure was uniformly applied to vector components of the magnetic field (B_X, B_Y, B_Z), bulk velocity (V_X, V_Y, V_Z), ion density (n_i), and ion temperature (T_i). Perturbations were computed by subtracting the filtered signal from the original (e.g., ($\Delta B = B\_\text{original} - B\_\text{filtered}$; $\Delta V = V\_\text{original}—V\_\text{filtered}$)). The resulting data set provides a clean separation between large-scale structure and dynamic fluctuations, ideal for both statistical analyses and targeted case studies. The 10-min filter window captures processes such as reconnection and substorms without suppressing mesoscale structures.

To quantify turbulence characteristics, we employed the db1 (Haar) wavelet from the Daubechies family, applying two complementary metrics:

Wavelet energy (E): Defined as the sum of squared wavelet coefficients, $E = \Sigma(C^2)$, where C^2 represents the wavelet coefficients. This metric identifies localized energy injections from intermittent events such as CS disruption or reconnection jets.

Wavelet entropy (H): derived from Shannon's entropy, this metric is given by: $H(k) = -\Sigma P \cdot \log(P + \epsilon)$, where $P = C^2/\text{Energy}$, and ϵ is a small constant to prevent singularities. This measure captures the signal's complexity and helps distinguish between organized and stochastic plasma behaviors.

3. Hybrid Filter-Decision Tree Region Partition Model

3.1. Model Constructing

The HFDTM, illustrated in Figure 1, is designed to classify plasma sheet regions using a physics-informed machine learning framework. The model processes three key plasma parameters: the magnetic field component (B_x), ion temperature (T_i), and plasma beta (β). Based on these inputs, it identified four characteristic regions in the magnetotail: CS, CPS, PSBL, and lobe. Note that the three physical parameters used in the HFDTM, namely B_x, β, and T_i, are either scalar quantities or individual vector components. As such, they are only minimally affected by coordinate transformations between GSE and GSM. Consequently, the HFDTM's region

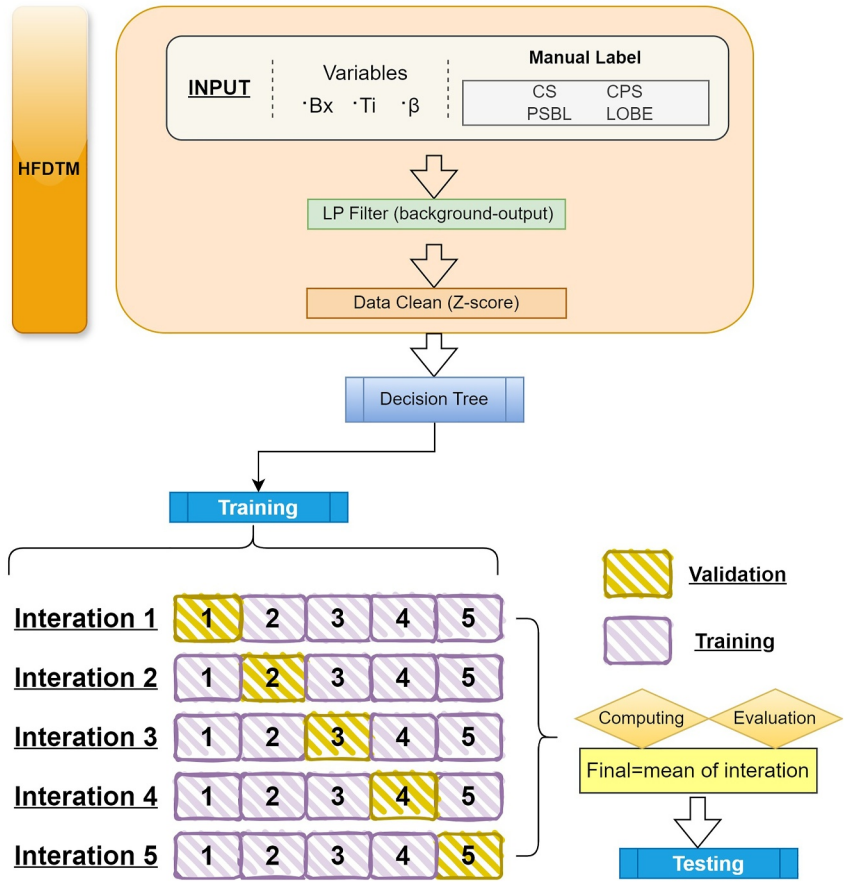

Figure 1. Schematic flowchart of the HFDTM. The model ingests key plasma parameters (B_X, T_i, β) and manually labeled region identifiers. Inputs are processed via low-pass filtering and *Z*-score normalization and then passed to a decision tree classifier trained with five-fold cross-validation. Final performance is assessed using averaged outputs from each fold on a holdout testing set.

classification remains effectively invariant, ensuring that the resulting partitioning and identification of magnetotail regions are both robust and coordinate-system independent.

The classification pipeline consists of two preprocessing stages:

1. *Low-pass filtering*: Used to extract large-scale background trends and suppress high-frequency noise while preserving mesoscale structures critical for regional discrimination.
2. *Z-score normalization*: Standardizes all input features to mitigate the impact of outliers and ensures uniform scaling across variables.

These preprocessed parameters are input into a decision tree classifier which dynamically partitions the magnetotail based on spatial variations in plasma properties.

3.2. Manual Labeling and Training Set Construction

Initial region labels were assigned based on statistical distributions of key plasma parameters, as visualized in Figure 2. Each region exhibits distinct physical characteristics. The CS shows highly dynamic with extreme plasma beta (median ≈ 100, IQR: 50–150), high ion temperatures (median ≈ 8,000 eV), and B_x values near zero, indicative of frequent reconnection and sheet flapping events. The CPS exhibits moderate turbulentity, with median $\beta \approx 50$ and $T_i \approx 5{,}000$ eV. PSBL behaves as transitional in nature, with decreasing β and T_i, reflecting intermediate variability. The lobe is the most quiescent region, characterized by low β (≈0.5), low T_i (≈500 eV), and strong, stable B_x (above 20 nT).

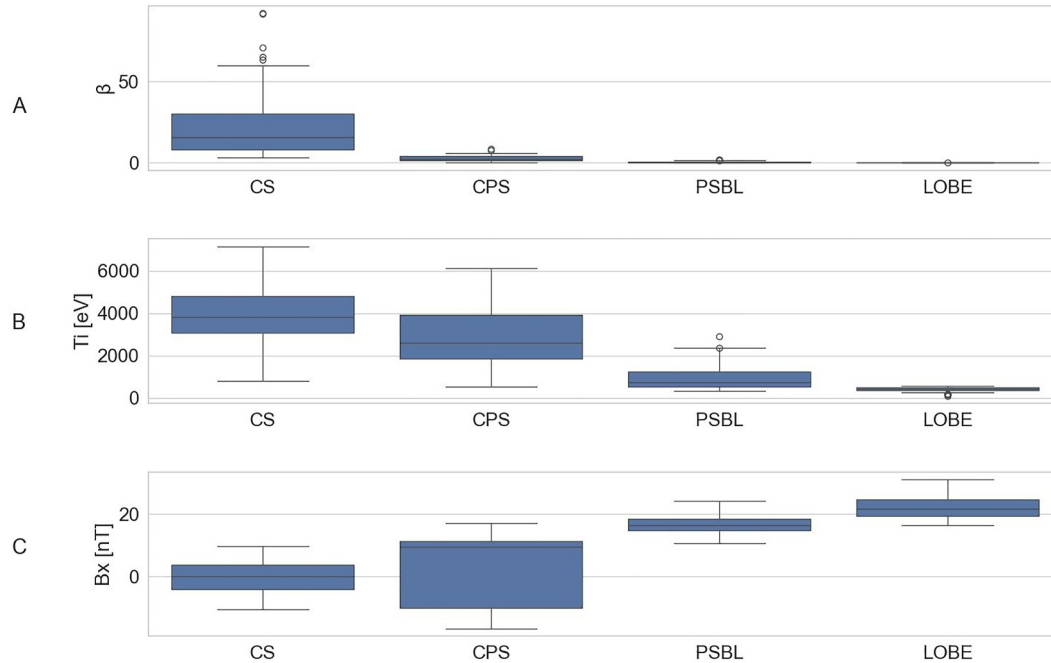

Figure 2. Box plots of key plasma parameters used for region classification: (a) Plasma beta (β), (b) ion temperature (T_i, eV), and (c) B_X (nT). Boxes show the interquartile range (IQR), medians as horizontal lines, whiskers extending to 1.5 × IQR, and outliers as dots. Strong regional separation and internal variability, especially in the current sheet and plasma sheet boundary layer, provide a robust foundation for classification.

The training data set was built from MMS observations between May and September 2017, with equal representation across regions. Each sample spans a 4-min interval to balance resolution and avoid temporal redundancy. Outliers were removed using a *Z*-score–based anomaly detection scheme. For each parameter (β, B_X, T_i), a composite anomaly score was calculated as: $A_i = \frac{1}{n}\sum_{j=1}^{n} Z_{ij}$, where A_i is the anomaly score for sample *i*, *n* is the number of features, and Z_{ij} is the Z-score for feature *j*. Samples with the highest scores were iteratively excluded until 100 clean samples remained per region. Notably, the PSBL exhibited the highest removal rate, consistent with its greater variability.

The cleaned data's statistical properties, illustrated in Figure 2, demonstrate clear separability among regions while preserving natural variability critical for the model to learn realistic boundaries. Panel A shows plasma β, with the CS displaying high variability and significant outliers, while other regions exhibit progressively lower and more stable values. Panel B displays ion temperature distributions highlighting elevated T_i in CS and CPS with a clear decline in PSBL and Lobe. Panel C illustrates the B_x component of the magnetic field. CS values cluster around zero, reflecting CS dynamics, while B_x increases steadily toward the lobe, indicative of stronger background fields (Table 1).

Table 1
Training Set Composition and Data Cleaning Summary

PS region	Samples		Removed (%)
	Before cleaning	After cleaning	
CS	108	100	7.4
CPS	113	100	11.5
PSBL	120	100	16.7
LOBE	109	100	8.25

Note. Sample counts before and after cleaning, along with percentage removed, are shown per region.

3.3. Feature Importance

To assess the relative contribution of each input parameter to region classification, we evaluated feature importance using normalized information gain, a standard metric in decision tree learning (Quinlan, 1986). Normalized information gain quantifies the reduction in entropy (i.e., uncertainty) resulting from a data split on a particular feature, scaled between 0 and 1. A higher value indicates that a feature contributes more effectively to distinguishing between classes. Entropy at each decision node is computed using a Shannon entropy-based formula: $H(k) = -\Sigma P \cdot \log(P + \epsilon)$, where $P = C^2/\text{Energy}$ and is a small constant to prevent singularities. This formulation captures the information complexity of turbulent plasma behavior across regions.

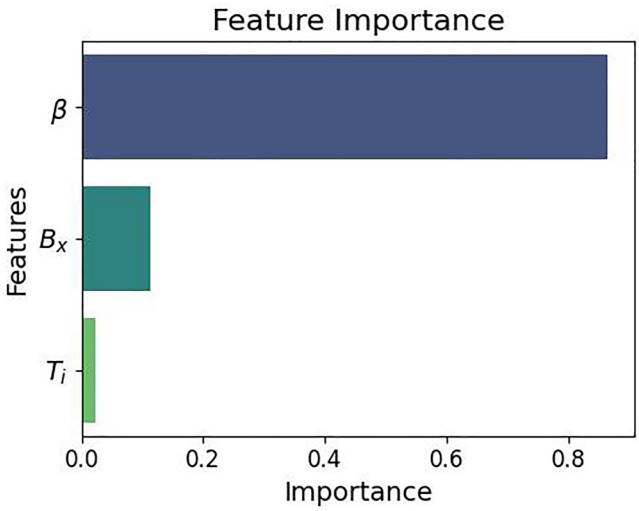

Figure 3. Feature importance ranking based on entropy reduction in the HFDTM. Plasma beta (β) is the most influential parameter (>85% weight), followed by B_X and T_i. This ranking aligns with theoretical expectations of plasma structure and regional boundaries in the magnetotail.

Table 2
Performance Comparison of Region Classification Models Applied to Magnetotail Plasma Sheet Data

Metric		Filter-based	Wavelet-based	Raw signal
CPS	precision	92.80%	84.20%	84.00%
	recall	92.00%	85.00%	80.00%
	f1-score	92.10%	83.40%	80.80%
CS	precision	99.10%	91.70%	88.40%
	recall	97.00%	90.80%	91.00%
	f1-score	98.00%	90.50%	89.20%
LOBE	precision	94.50%	95.40%	94.40%
	recall	96.00%	98.00%	95.00%
	f1-score	95.00%	96.50%	94.60%
PSBL	precision	89.50%	92.80%	87.00%
	recall	89.00%	87.00%	84.00%
	f1-score	88.80%	89.20%	84.70%
Accuracy		93.70%	90.20%	87.60%
Macro Avg	precision	94.00%	91.10%	88.30%
	recall	93.50%	90.20%	87.60%
	f1-score	93.30%	89.90%	87.40%
Weighted Avg	precision	94.00%	91.10%	88.30%
	recall	93.60%	90.20%	87.60%
	f1-score	93.30%	89.90%	87.40%

Note. Results are presented for three approaches: filter-based (HFDTM), wavelet-based (WDTM), and raw signal input. For each magnetotail region (CS, CPS, PSBL, LOBE), precision, recall, and F1-scores are reported. Aggregate performance metrics, including overall accuracy, macro-averaged, and weighted-average scores, are also included.

As shown in Figure 3, β is the most informative feature (≈0.8), reflecting its dominant role in defining pressure balance across magnetotail regions. B_x and T_i showed moderate importance (≤0.3), contributing additional discriminatory power.

3.4. Performance Evaluation

Model performance was evaluated using standard classification metrics, including precision, recall, F1-score, and overall accuracy (Sokolova & Lapalme, 2009). These metrics are widely adopted in classification tasks, including plasma region identification in space physics (Nguyen et al., 2022; Wang et al., 2025). Specifically, precision quantifies the proportion of correctly predicted samples among all predicted instances of a given region; recall measures the proportion of correctly identified samples among all actual instances of that region; and the F1-score, defined as the harmonic mean of precision and recall, provides a balanced assessment of classification accuracy.

To evaluate the robustness of the HFDTM, we benchmarked its performance against two alternative approaches: (a) a Wavelet-based Decision Tree Model (WDTM) (Wang et al., 2025), and (b) a baseline classifier using raw signal input without preprocessing. Comparative results are summarized in Table 2.

From Table 2, the HFDTM achieved the highest performance, with 93.7% accuracy and a macro F1-score of 93.3%, outperforming both alternatives. Its advantage is particularly pronounced in dynamic zones, such as the CS and CPS, where mesoscale fluctuations are critical. The raw-signal approach performed worst overall (87.6% accuracy), especially in the CPS (F1 ≈ 80.8%), underscoring the importance of preprocessing. The HFDTM thus emerges as a reliable method for region classification in the plasma sheet, combining high statistical accuracy with physical interpretability. Its architecture preserves the mesoscale structure while filtering noise, making it especially effective in turbulent or transitional regimes.

4. Magnetic and Velocity Fluctuations in the Plasma Sheet: β-Dependence

To examine the evolution of magnetic and plasma fluctuations with respect to plasma β in Earth's magnetotail, we analyzed a data set comprising 127,959 one-minute-averaged intervals from MMS1. These intervals were collected during tailward crossings ($X < -10$ R_E) from May to September 2017.

4.1. Magnetic Field Variability Across β

Figure 4 illustrates the β-dependent morphology of the background magnetic field components (B_{X0}, B_{Y0}, B_{Z0}). B_{X0} (Panel a) exhibits a symmetric, fork-like structure centered around zero, with magnetic intensity decreasing as plasma β increases. This configuration is characteristic of a Harris-type CS and reflects the stretched magnetic topology of the mid-tail region. B_{Y0} (Panel c) forms a bullet-shaped, symmetric distribution centered near zero, constrained within ±20 nT, suggesting a stable dawn–dusk component likely associated with global current systems and/or IMF-B_Y penetration. B_{Z0} (Panel e) displays a horizontally extended profile ranging from 0 to 15 nT, with a distinct two-hump structure: a positive hump at intermediate β (0.5–5) and a broader negative hump at higher β (1–10), likely reflecting the presence of embedded flux tubes and transient features such as dipolarization fronts and tailward reconnection exhausts.

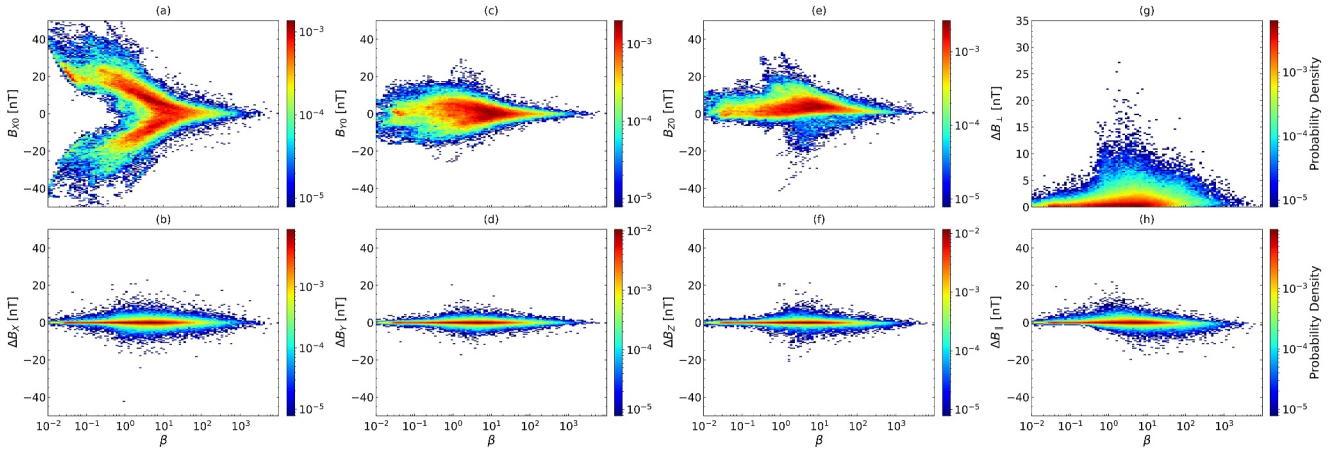

Figure 4. Two-dimensional probability distributions of background and fluctuating magnetic field components as a function of plasma β, based on MMS1 one-minute intervals ($X < -10$ R_E). (a) B_{X0}, (b) ΔB_X, (c) B_{Y0}, (d) ΔB_Y, (e) B_{Z0}, (f) ΔB_Z, (g) $\Delta B_\perp$, and (h) $\Delta B_{//}$. Color scales denote probability density, with warmer colors (e.g., red) indicating higher density.

The magnetic fluctuation components (ΔB_X, ΔB_Y, ΔB_Z, $\Delta B_\perp$, $\Delta B_\parallel$) also exhibit pronounced β-dependence. ΔB_X (Panel b) peaks around ±20 nT in the CPS ($\beta \approx 1$–10), with a zero-centered distribution suggesting frequent small perturbations interspersed with intermittent strong events. In ultra-low-β environments ($\beta < 0.1$), typical of the lobe and outer PSBL, ΔB_X remains subdued (<5 nT), while modest enhancement in low-β regimes ($0.1 < \beta < 1$) indicates increasing variability. ΔB_Y and ΔB_Z (Panels d and f) (Panels d and f) show symmetric distributions with peak amplitudes around 15–20 nT, also intensifying in the CPS. $\Delta B_\perp$ (Panel g) dominates in the medium-β range ($\beta \approx 1$–20), with amplitudes largely within 0–5 nT, consistent with Alfvénic or coherent structural turbulence where energy transfer is predominantly across field lines. In contrast, $\Delta B_\parallel$ (Panel h) is generally weaker (<15 nT) but exhibits a systematic polarity reversal: positive in low-β regions (PSBL, lobe) and negative in higher β environments (CPS, CS), indicating a transition from field-aligned expansion to compressive dynamics.

4.2. Plasma Flow and Thermodynamic Response

Figure 5 presents β-dependent trends in plasma flow velocities, ion density, and temperature, both background and fluctuates. $V_{\perp 0}$ (Panel 5a) ranges from 0 to 600 km/s, peaking mostly below 100 km/s across $\beta \approx 0.01$–100, consistent with stagnant to moderate flows. Secondary structures between 200 and 400 km/s ($\beta \approx 10$–100) and near 600 km/s ($\beta \approx 1$–10) are likely reconnection jets or dipolarization flows. Distinct structures at 200–400 km/s ($\beta \approx 10$–100) and ~600 km/s ($\beta \approx 1$–10) likely correspond to reconnection jets or dipolarization flow. $\Delta V_\perp$ (Panel

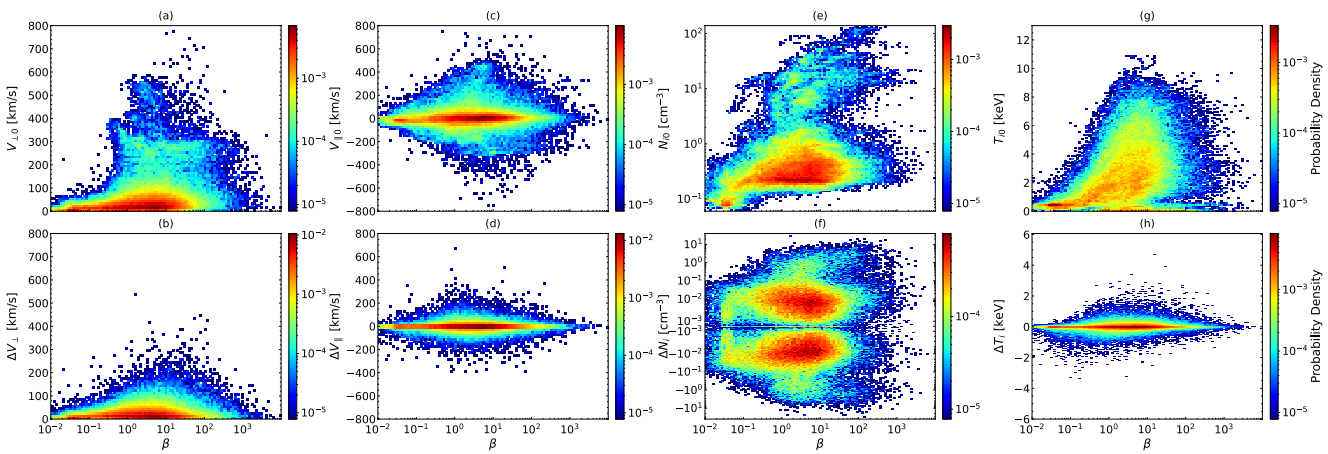

Figure 5. Two-dimensional probability distributions of background and fluctuating plasma parameters as a function of plasma β. (a) $V_{\perp 0}$, (b)$\Delta V_\perp$, (c) $V_{\parallel 0}$, (d) $\Delta V_\parallel$, (e) n_{i0}, (f) Δn_i, (g) T_{i0}, and (h) ΔT_i. Warmer colors indicate higher probability density.

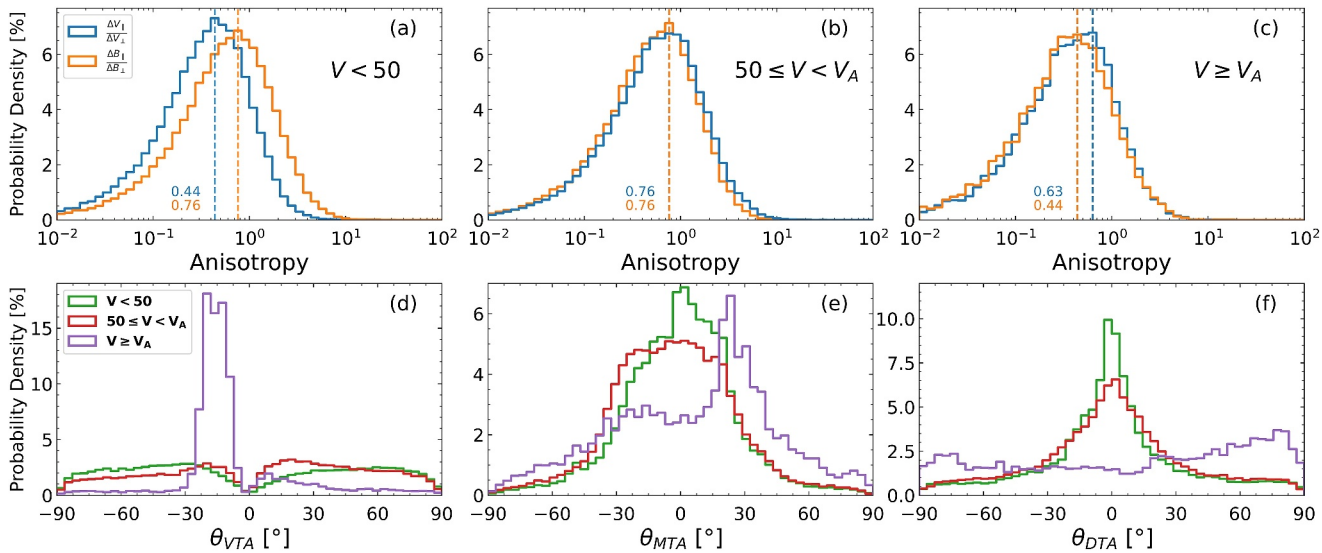

Figure 6. Evolution of velocity and magnetic field anisotropy (top row) and tilt angles (bottom row) across flow regimes: stagnant (green), sub-Alfvénic (red), and super-Alfvénic (purple). Panels (a–c): ($\Delta V_{\parallel}/\Delta V_{\perp}$, blue) and magnetic anisotropy ($\Delta B_{\parallel}/\Delta B_{\perp}$, orange). Panels (d–f): θ_{VTA} ($= \arctan(\frac{\sqrt{V_Y^2+V_Z^2}}{V_X})$), θ_{MTA} ($= \arctan\left(\frac{B_Y}{B_X}\right)$), and θ_{DTA} ($= a \arctan(\frac{B_Z}{B_X})$). Vertical dashed lines denote peak location.

b) shows a broad hump below 400 km/s, indicative of mesoscale fluctuations embedded within the background convection. $V_{\parallel 0}$ (Panel 5c) displays a symmetric range from −600 to +600 km/s, peaking near zero, reflecting balanced field-aligned flows. $\Delta V_{\parallel}$ (Panel 5d) is also symmetric, but its amplitude increases at moderate β (1–10), pointing to eddy-like disturbances within bursty flows and/or dipolarization flow (e.g., Zhang, Baumjohann, et al., 2015; Zhang, Dai, et al., 2015; Zhang, Wang, et al., 2015; Ukhorskiy et al., 2022).

Ion density (n_{i0}) and its fluctuation (Δn_i) vary strongly with β. n_{i0} (Panel 5e) ranges from 0.1 to 100 cm^{-3}, peaking around 1–10 cm^{-3}, consistent with CPS norms. Δn_i (Panel 5f) spans a wide range (10^{-2}–10^2 cm^{-3}) with a bipolar profile, suggesting simultaneous compressional and rarefactional dynamics, likely due to turbulence. T_{i0} (Panel 5g) varies between 0 and 12 keV and peaks at 1–5 keV, indicative of a mostly thermalized plasma. ΔT_i (Panel h) presents a skewed bipolar structure, with sharp cooling (−6 keV) near $\beta \approx 1$ and broader heating (∼+6 keV) near $\beta \approx 5$, attributed to adiabatic expansion and localized reconnection heating in the CPS, respectively.

4.3. Identification of a Transitional Regime

Collectively, the results identify the $\beta \approx 1$–10 interval as a transitional regime where the magnetotail departs from global equilibrium and becomes increasingly dynamic. This regime is marked by amplified magnetic and plasma fluctuations, concurrent heating and cooling events, and multiscale coupling from global Harris-type sheets (≥10 R_E) to mesoscale (∼1,000 km) and kinetic-scale (<ion inertial length) structures. Although global ordering persists, turbulence becomes increasingly anisotropic and fragmented, highlighting β as a pivotal control parameter in magnetotail dynamics.

5. Statistical Results

5.1. Anisotropy Across Flow Regimes

Figure 6 presents statistical distributions of velocity and magnetic field anisotropy, along with tilt angle metrics, across three flow regimes: stagnant ($V < 50$ km/s), sub-Alfvénic ($50 \le V < V_A$), and super-Alfvénic ($V \ge V_A$). In the stagnant regime (Panel a), both $\Delta V_{\parallel}/\Delta V_{\perp}$ and $\Delta B_{\parallel}/\Delta B_{\perp}$ cluster near unity, with median values around 0.44 and 0.76, respectively, reflecting a quiescent and near-isotropic plasma environment.

As flow transitions into the sub-Alfvénic regime (Panel 6b), velocity anisotropy remains stable, while magnetic anisotropy shows a slight decrease, indicating early structural reorientation. This suggests that even moderate

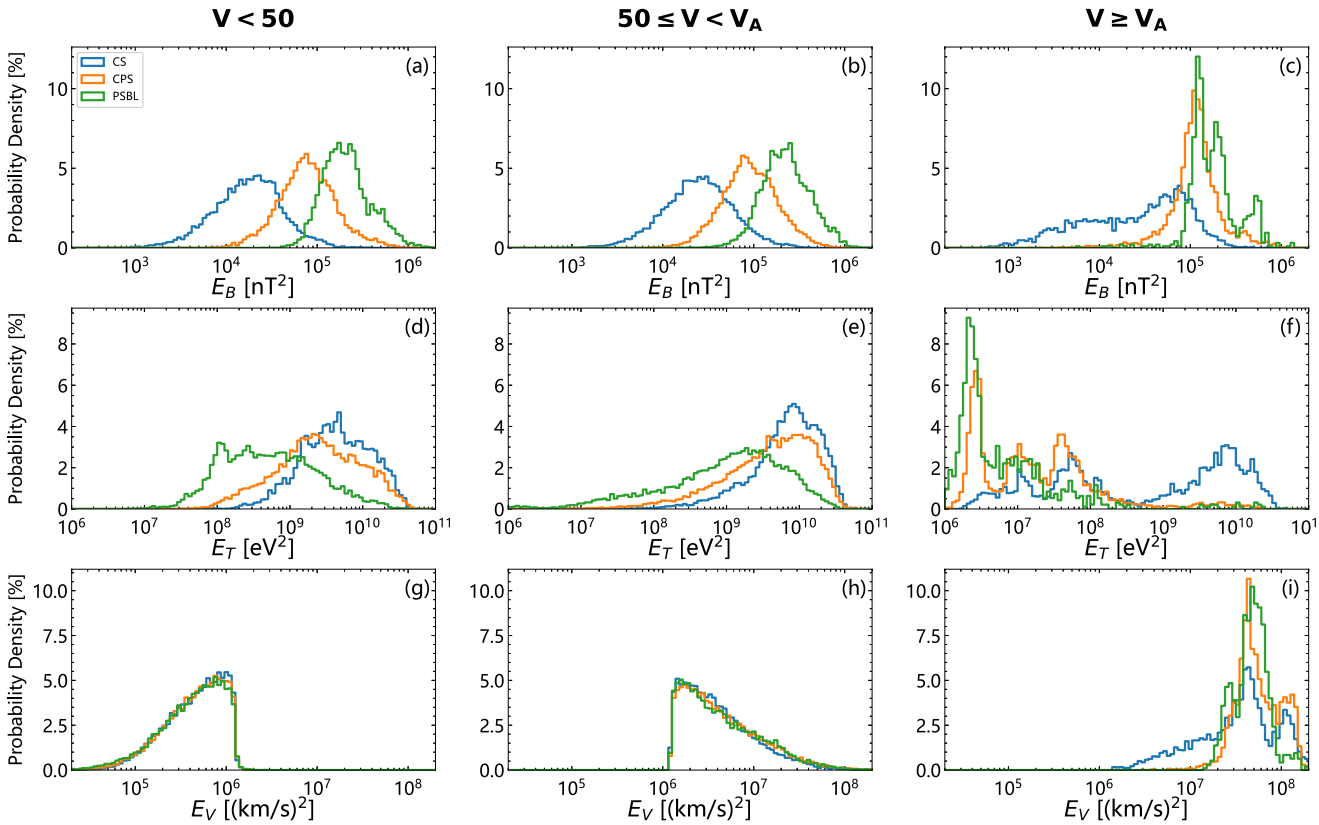

Figure 7. Evolution of wavelet energy densities across magnetic field (E_B), ion temperature (E_T), and ion velocity (E_V) components under different flow regimes. From top to bottom, panels (a–c) show magnetic field energy, (d–f) show ion temperature energy, and (g–i) show ion velocity energy. Each column corresponds to a distinct flow category: stagnant ($V < 50$ km/s), sub-Alfvénic ($50 \leq V < V_A$), and super-Alfvénic ($V \geq V_A$). Curves represent distributions from the current sheet (CS, blue), central plasma sheet (CPS, orange), and plasma sheet boundary layer (PSBL, green).

flows begin perturbing the magnetic field more than the velocity field, likely signaling the accumulation of internal stresses or weak reconnection activity.

In the super-Alfvénic regime (Panel 6c), anisotropy values decline markedly. Magnetic anisotropy falls to a median of ∼0.44, while velocity anisotropy drops to ∼0.63, reflecting a growing dominance of perpendicular fluctuations. This trend aligns with the onset of fully developed turbulence and magnetic disorder, especially within BBFs. The more significant disruption of magnetic fields implies their higher sensitivity to turbulent deformation.

The angular tilt distributions (Panels 6d–6f) further support this interpretation. θ_{VTA} and θ_{MTA} remain tightly centered around 0° under stagnant and sub-Alfvénic flows, indicating radial-aligned structures. However, in the super-Alfvénic regime, θ_{VTA} broadens to ±60°, and θ_{MTA} becomes bimodal (±30°), evidencing multidirectional plasma motion and magnetic kinking. Conversely, θ_{DTA} remains sharply peaked at around 0° in all regimes, suggesting that the vertical dipolar structure remains intact and largely unaffected by horizontal turbulence.

In summary, magnetic anisotropy evolves from near-isotropic ($\Delta B_{\parallel}/\Delta B_{\perp} \approx 1.1$) to strongly perpendicular-dominated (∼0.4) with increasing flow speed. Velocity anisotropy shows a more gradual decline (∼0.8–∼0.5). These trends highlight the magnetic field's greater vulnerability to turbulent deformation and the transition to multidirectional dynamics in super-Alfvénic flow regimes.

5.2. Wavelet Energy Distributions

Figure 7 illustrates the evolution of wavelet energy in magnetic (E_B), thermal (E_T), and kinetic (E_V) components across regions and flow regimes. E_B consistently ranks highest in the PSBL, intermediate in the CPS, and lowest in the CS. In the stagnant regime (Panels 7a), E_B spans from approximately 10^3 to 10^6 nT^2, with region-specific

peaks around $10^{4.1}$ nT^2 in the CS, $10^{4.8}$ nT^2 in the CPS, and $10^{5.2}$ nT^2 at the PSBL. When transitioning into the sub-Alfvénic regime (Panel 7b), these distributions remain broadly similar, indicating that sub-Alfvénic flow introduces only minor adjustments to magnetic energy structure. However, under super-Alfvénic conditions (Panel 7c), all components exhibit pronounced amplification. E_B reaches $\sim10^{4.6}$ nT^2 in the CS, $\sim10^{4.8}$ nT^2 in the CPS, and $\sim10^{5.0}$ nT^2 in the PSBL. Notably, the PSBL develops an extended high-energy tail exceeding $10^{5.1}$ nT^2, signifying turbulence injection and cascading.

E_V distributions mirror this dynamic. In the stagnant regime (Panel 7g), E_V remains below 10^6 (km/s)^2 and shows a narrow Gaussian-like profile centered around $10^{5.8}$ (km/s)^2, with minimal variance among the CS, CPS, and PSBL. Entering the sub-Alfvénic regime (Figure 7h), the E_V distributions shift upward significantly, ranging from $\sim10^6$ to 10^8 (km/s)^2, although inter-region variance remains modest. Under super-Alfvénic conditions (Panel 7i), E_V becomes highly asymmetric. The CS spans from $\sim10^6$ to 10^8 (km/s)^2, while both the CPS and PSBL extend from $\sim10^7$ to 10^8 (km/s)^2. These latter regions dominate the enhancement, peaking at $\sim10^{7.5}$ (km/s)^2, consistent with reconnection-driven outflows and shear turbulence.

E_T reveals complex thermodynamic behavior. In stagnant flow (Panel 7d), E_T ranges from 10^7 to 10^{10} eV^2. Interestingly, E_T exhibits an inverse spatial profile compared to E_B. It peaks in the CS ($\sim10^{9.5}$ eV^2), is slightly lower in the CPS ($\sim10^{9.1}$ eV^2), and is the lowest in the PSBL ($\sim10^{7.5}$ eV^2). As the flow intensifies, heating becomes more distributed. With the onset of sub-Alfvénic flow (Panel 7e), all components shift upward: the PSBL to $\sim10^{9.1}$ eV^2, the CPS to $\sim10^{9.5}$ eV^2, and the CS to $\sim10^{10.7}$ eV^2. Under super-Alfvénic conditions (Panel 7f), multimodal structures appear. In the CS, three distinct peaks appear at $\sim10^7$, $\sim10^{7.5}$, and $\sim10^{10}$ eV^2. The CPS also displays tri-modal behavior, with peaks at $\sim10^{6.1}$, $\sim10^7$, and $\sim10^{7.3}$ eV^2. In contrast, the PSBL shows a sharp unimodal peak at $\sim10^{6.2}$ eV^2 without substructure.

5.3. Wavelet Enstrophy Distributions

Figure 8 presents the wavelet enstrophy (H) distributions for magnetic (H_B), thermal (H_T), and kinetic (H_V) domains. H_B peaks in the PSBL across all regimes, expanding into the CPS and CS under faster flows. In the stagnant flow regime, H_B exhibits a sharp peak at $H_B \approx 3.401$, narrowly concentrated on the PSBL. Under sub-Alfvénic conditions, the CPS develops a broader secondary peak around $H_B \approx 3.41$, while CS shows a distinct peak at ~3.38, evidence of localized turbulence and magnetic structuring expanding inward from the boundary. In the super-Alfvénic regime, H_B distribution becomes markedly broadened, extending from $H_B \approx 3.400$ to 3.304, consistent with increased magnetic complexity and cascading.

H_V (Panels 7g–7i) captures the intermittent and vortical nature of flow dynamics. In contrast to H_B, H_V is lowest in the PSBL and higher in the CS and CPS. A regime-dependent transition is observed in both stagnant and sub-Alfvénic regimes. The CS is the primary source of H_V. However, under super-Alfvénic conditions, dominance shifts to the CPS, indicating intensified flow shear and nonlinear mixing processes in the central plasma region.

H_T evolves in a similar pattern to H_V. It transitions from CS-dominance under stagnant conditions to CPS-dominance in super-Alfvénic flow, mirroring the trends seen in kinetic energy. This tight coupling between thermal and velocity enstrophy implies that chaotic, intermittent heating is more tightly regulated by flow structures than magnetic ones, reinforcing the view that turbulence and energy conversion in the super-Alfvénic flow are primarily governed by velocity shear-driven rather than purely wave-associated processes.

6. Discussion

The multimodal thermal energy distributions in the CS and CPS during super-Alfvénic flow (Figure 7f) suggest the operation of dual energy transfer pathways, kinetic and magnetic, acting simultaneously. This interpretation is further supported by the wavelet enstrophy analysis (Figure 8), where H_T and H_V evolve in parallel and shift spatially from the CS to the CPS as the flow speed increases. In contrast, H_B consistently peaks in the PSBL across all flow regimes. These observations support the hypothesis that intermittent heating is predominantly governed by flow structures, particularly those generated by reconnection, turbulence, and velocity shear dynamics.

Figure 9 provides a compelling statistical breakdown of correlation strengths between velocity and magnetic field components across various plasma regimes and spatial regions within the magnetotail, offering critical insights into the underlying turbulence mechanisms. A dominant observation is that weak-to-moderate correlations overwhelmingly characterize the system, with correlation coefficients (|CC|) below 0.7 accounting for over 85%–

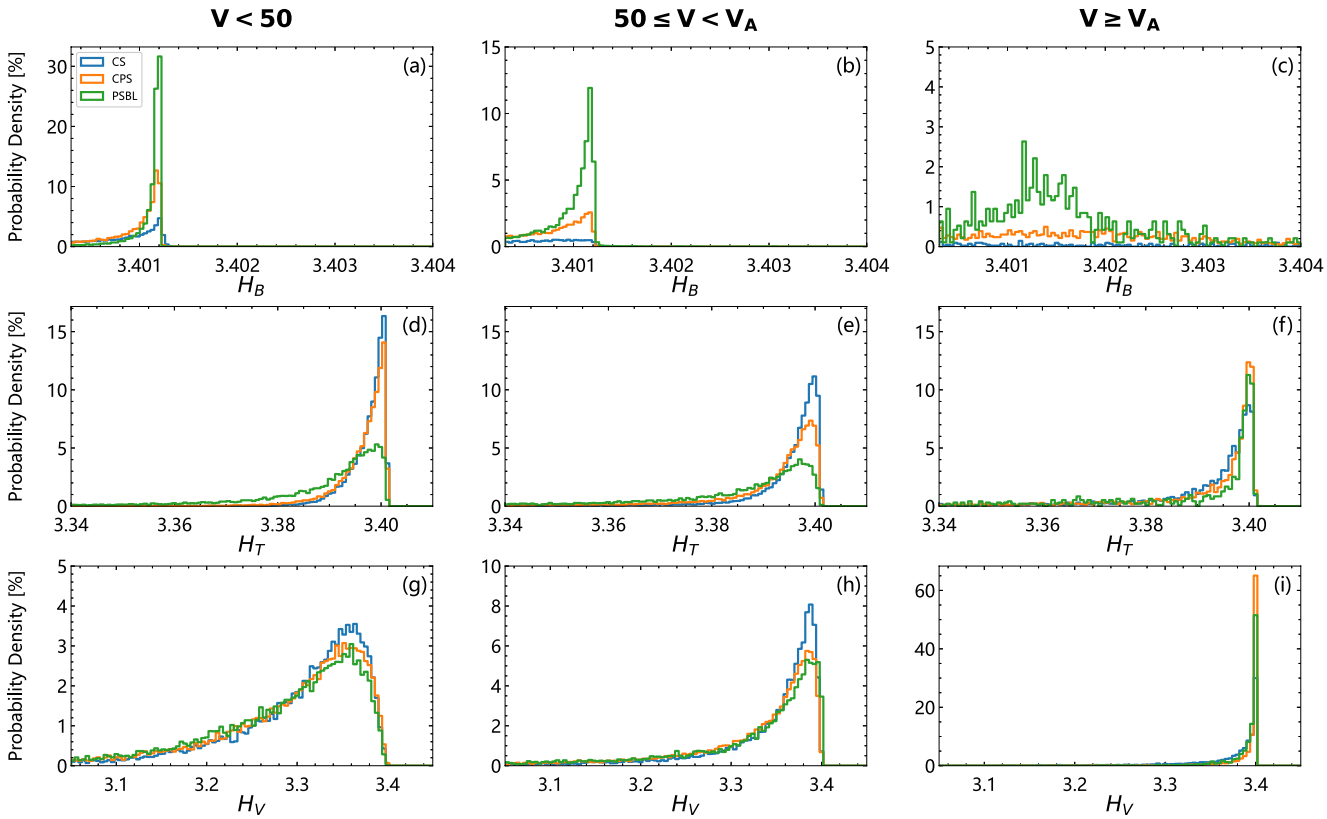

Figure 8. Evolution of wavelet enstrophy (H) distributions across different plasma parameters and flow regimes. Top row (a–c): magnetic field enstrophy (H_B); middle row (d–f): ion temperature enstrophy (H_T); bottom row (g–i): ion velocity enstrophy (H_V). Columns represent stagnant ($V < 50$ km/s), sub-Alfvénic ($50 \leq V < V_A$), and super-Alfvénic ($V \geq V_A$) conditions. Color coding corresponds to current sheet (CS, blue), central plasma sheet (CPS, orange), and plasma sheet boundary layer (PSBL, green).

93% of the events across all examined cases. This predominance of lower correlation strengths is consistent throughout the CS, CPS, and PSBL, and across all flow regimes from sub-Alfvénic to super-Alfvénic. Such widespread incoherence supports the interpretation that magnetotail turbulence is not governed by classical MHD wave processes but is instead highly intermittent and fragmented, driven by short-lived structures such as dipolarization fronts, flow decelerating/braking, and localized reconnection events (Fu et al., 2012a, 2012b; Zhang, Lui, et al., 2020). These findings affirm the departure from coherent Alfvénic wave activity and align well with the multiscale bursty nature of plasma dynamics documented in observational works such as those of Volwerk et al. (2004), Wang et al. (2016), and Šafránková et al. (2021).

A component-wise assessment reveals a balanced occurrence of transverse (Alfvénic) and compressive (non-Alfvénic) couplings. Specifically, $V_\perp$–$B_\perp$ and $V_\perp$–$B_\parallel$ pairs capture shear Alfvénic and possible kinetic Alfvén wave interactions, while $V_\parallel$–$B_\perp$ interactions are representative of slow-mode compression and mirror mode activity. However, of particular note are the $V_\parallel$–$B_\parallel$ pairings, which consistently stand out in the strong correlation bins ($|CC| \geq 0.7$) across all flow regimes and spatial locations. In the super-Alfvénic regime, $V_\parallel$–$B_\parallel$ reaches the highest strong correlation levels, peaking at over 10% in the CS, significantly higher than other component pairs. This statistically significant enhancement in $V_\parallel$–$B_\parallel$ coupling under high-speed flow conditions suggests a shift in the dominant transport mechanism away from traditional Alfvénic turbulence toward field-aligned energy transport processes. The increased coherence of these interactions likely reflects the influence of structured field-aligned flows, such as those induced by anisotropic pressure gradients, mirror mode instabilities, or kinetic slow shocks, which are often outside the scope of standard MHD turbulence theory.

These statistical findings on the V–B correlation strength are further corroborated by the wavelet energy and enstrophy analyses. Under super-Alfvénic conditions, the wavelet energy distributions for magnetic, kinetic, and thermal components exhibit broad, asymmetric, and often multi-peaked structures, especially within the CPS and

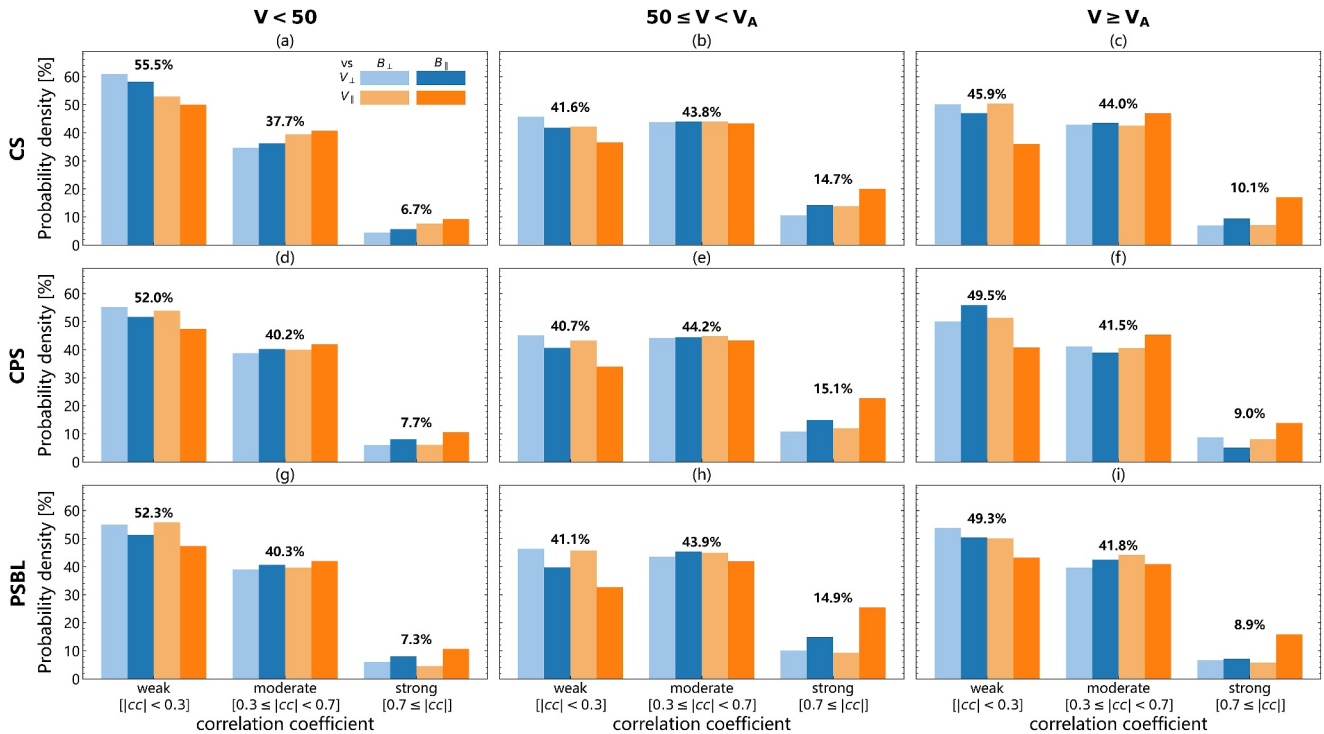

Figure 9. Correlation strength distributions between velocity and magnetic perturbations in the plasma sheet, evaluated across the current sheet, central plasma sheet, and plasma sheet boundary layer. Top and bottom rows show $V_{\perp}$-dominant and $V_{\parallel}$-dominant cases, respectively. Correlation coefficients (CC) are categorized into three bins: weak (|CC| < 0.3), moderate (0.3 ≤ |CC| < 0.7), and strong (|CC| ≥ 0.7). The top and bottom panels correspond to perpendicular ($V_{\perp}$-dominant) and parallel ($V_{\parallel}$-dominant) velocity fluctuation cases, respectively. Four correlation pairings are shown: $V_{\perp}$–$B_{\perp}$ (light blue), $V_{\perp}$–$B_{\parallel}$ (dark blue), $V_{\parallel}$–$B_{\perp}$ (light orange), and $V_{\parallel}$–$B_{\parallel}$ (dark orange), capturing both transverse (Alfvénic) and compressive (field-aligned) interaction channels. Correlation probabilities are normalized and sum to unity for each panel.

PSBL. These distributions are characteristic of intermittent turbulence, where energy is transferred through localized bursts rather than continuous homogeneous fluctuations. Similarly, the enstrophy distributions reveal broadened magnetic enstrophy (H_B) and a flow-regime-dependent shift in the dominance of kinetic (H_V) and thermal (H_T) enstrophy from the CS to the CPS. This pattern reflects intensified flow shear, enhanced mixing, and small-scale structuring, particularly in the central and boundary layer regions. These wavelet-based signatures of complexity and localization are consistent with the predominance of weak-to-moderate *V–B* correlations. Together, these results confirm that energy transfer in the magnetotail is largely governed by fragmented, short-lived processes rather than coherent Alfvénic coupling. They reinforce the interpretation that enhanced intermittency, driven by magnetic reconnection, substorm dipolarization, and flow braking, is a fundamental feature of the plasma sheet's turbulent environment.

Overall, these findings imply that the magnetotail does not conform to a single turbulence paradigm. Instead, it constitutes a hybrid environment where multiple interaction mechanisms coexist and evolve dynamically with changing flow conditions. The reversal of magnetic field anisotropy, the emergence of multimodal heating signatures, and the enhanced $V_{\parallel}$–$B_{\parallel}$ correlations, particularly during BBF turbulence, point to a departure from classical Alfvénic turbulence, which is predominantly transverse and anisotropic. These results highlight the importance of incorporating non-Alfvénic, field-aligned structures and non-equilibrium processes into models of plasma sheet turbulence.

7. Conclusions

In this study, we present a comprehensive, regionally resolved investigation of magnetic and velocity fluctuations in Earth's magnetotail plasma sheet, enabled by the application of a machine learning-based magnetotail classifier (HFDTM). This classifier facilitates a flow-regime–aware diagnostic framework, allowing us to examine fluctuations across the CS, CPS, and PSBL under varying plasma flow conditions. The results reveal a fundamentally

multiscale and anisotropic system, whose behavior is strongly governed by both plasma flow speed and spatial localization. The key findings of the study are summarized as follows:

1. Anisotropy Transition: Magnetic field anisotropy reverses with increasing flow speed from near-isotropic values ($\Delta B_{\parallel}/\Delta B_{\perp} \approx 1.1$) under stagnant conditions to strongly perpendicular-dominated distributions (∼0.4) in the super-Alfvénic regimes. Velocity anisotropy shows a more gradual shift (∼0.8–∼0.5), indicating stronger sensitivity of magnetic structures to flow deformation.
2. Multimodal Heating: Wavelet energy and enstrophy analyses reveal multi-peak structures in the thermal energy spectrum, particularly under super-Alfvénic flow conditions. Diverging trends between E_B and E_V the nonequivalence of magnetic and kinetic energy transfer under strong driving. A pronounced spatial discrepancy between H_B and H_T, alongside the close correspondence H_T–H_V evolution, confirms the role of eddy-driven heating and supports the presence of dual energy transfer pathways, magnetic and kinetic, that together give rise to the observed multimodal heating behavior.
3. Correlation structure: Across all regions and flow regimes, weak-to-moderate velocity–magnetic field (V–B) correlations dominate, suggesting enhanced intermittency in plasma sheet turbulence. However, under super-Alfvénic conditions, $V_{\parallel}$–$B_{\parallel}$ interactions emerge as the dominant source of strong correlation, signaling a transition toward more coherent field-aligned energy transport mechanisms.

Data Availability Statement

The MMS data sets analyzed during the current study are available in the [CDAWEB] repository, https://cdaweb.gsfc.nasa.gov/pub/data/mms/ The WIND data sets are available through the link: https://cdaweb.gsfc.nasa.gov/pub/data/WIND/ (accessed on 10 November 2024).

Acknowledgments
We would like to thank the PIs and those who contributed to the success of the MMS mission. Data analysis was performed using the IRFU-Matlab analysis package (version 1.16.3) available at https://github.com/irfu/irfu-matlab. Project Supported by the Specialized Research Fund for State Key Laboratory of Solar Activity and Space Weather. This work is supported by NNSFC Grants (42374198, 42188101), the project of Civil Aerospace "14th Five Year Plan" Preliminary Research in Space Science (D010301, D010202). H. Li is also supported by the International Partnership Program of CAS (Grant 183311KYSB20200017).

References

Baker, D. N., Pulkkinen, T. I., Angelopoulos, V., Baumjohann, W., & McPherron, R. L. (1996). Neutral line model of substorms: Past results and present view. *Journal of Geophysical Research*, *101*(A6), 12975–13010. https://doi.org/10.1029/95JA03753

Baumjohann, W., Hesse, M., Kokubun, S., Mukai, T., Nagai, T., & Petrukovich, A. A. (1999). Substorm dipolarization and recovery. *Journal of Geophysical Research*, *104*(A11), 24995–25000. https://doi.org/10.1029/1999JA900282

Baumjohann, W., Paschmann, G., & Lühr, H. (1990). Pressure balance between lobe and plasma sheet. *Geophysical Research Letters*, *17*(1), 45–48. https://doi.org/10.1029/GL017i001p00045

Bendt, A., Chapman, S., & Dudok de Wit, T. (2024). The relative prevalence of wave packets and coherent structures in the inertial and kinetic ranges of turbulence as seen by Solar Orbiter. *The Astrophysical Journal*, *971*(2), 179. https://doi.org/10.3847/1538-4357/ad54bc

Borovsky, J. E., & Bonnell, J. (2001). The dc electrical coupling of flow vortices and flow channels in the magnetosphere to the resistive ionosphere. *Journal of Geophysical Research*, *106*(A12), 28967–28994. https://doi.org/10.1029/1999JA000245

Borovsky, J. E., Elphic, R. C., Funsten, H. O., & Thomsen, M. F. (1997). The Earth's plasma sheet as a laboratory for flow turbulence in high-β MHD. *Journal of Plasma Physics*, *57*, 1–34. https://doi.org/10.1017/S0022377896005259

Borovsky, J. E., & Funsten, H. O. (2003). MHD turbulence in the Earth's plasma sheet: Dynamics, dissipation, and driving. *Journal of Geophysical Research*, *108*(A7), 1284. https://doi.org/10.1029/2002JA009625

Bruno, R., & Carbone, V. (2013). The solar wind as a turbulence laboratory. *Living Reviews in Solar Physics*, *10*(2), 1–160. https://doi.org/10.12942/lrsp-2013-2

Burch, J., Moore, T., Torbert, R., & Giles, B. (2016). Magnetospheric multiscale overview and science objectives. *Space Science Reviews*, *199*(1–4), 5–21. https://doi.org/10.1007/s11214-015-0164-9

Cheng, C. (2004). Physics of substorm growth phase, onset, and dipolarization. *Space Science Reviews*, *113*(1/2), 207–270. https://doi.org/10.1023/B:SPAC.0000042943.59976.0e

Coppi, B., Laval, G., & Pellat, R. (1966). Dynamics of the geomagnetic tail. *Physical Review Letters*, *16*(26), 1207–1209. https://doi.org/10.1103/PhysRevLett.16.1207

El-Alaoui, M., Richard, R. L., Ashour-Abdalla, M., Goldstein, M. L., & Walker, R. J. (2013). Dipolarization and turbulence in the plasma sheet during a substorm: THEMIS observations and global MHD simulations. *Journal of Geophysical Research: Space Physics*, *118*(12), 7752–7761. https://doi.org/10.1002/2013JA019322

El-Alaoui, M., Walker, R. J., Weygand, J. M., Lapenta, G., & Goldstein, M. L. (2021). Magnetohydrodynamic turbulence in the Earth's magnetotail from observations and global MHD simulations. *Frontiers in Astronomy and Space Sciences*, *8*, 620519. https://doi.org/10.3389/fspas.2021.620519

Ergun, R. E., Goodrich, K. A., Wilder, F. D., Ahmadi, N., Holmes, J. C., Eriksson, S., et al. (2018). Magnetic reconnection, turbulence, and particle acceleration: Observations in the Earth's magnetotail. *Geophysical Research Letters*, *45*(8), 3338–3347. https://doi.org/10.1002/2018GL076993

Fu, H. S., Khotyaintsev, Y. V., Vaivads, A., André, M., & Huang, S. Y. (2012a). Electric structure of dipolarization front at sub-proton scale. *Geophysical Research Letters*, *39*(6), L06105. https://doi.org/10.1029/2012GL051274

Fu, H. S., Khotyaintsev, Y. V., Vaivads, A., André, M., & Huang, S. Y. (2012b). Occurrence rate of earthward-propagating dipolarization fronts. *Geophysical Research Letters*, *39*(10), L10101. https://doi.org/10.1029/2012GL051784

Gonzalez, W. D., & Mozer, F. S. (1974). A quantitative model for the potential resulting from reconnection with an arbitrary interplanetary magnetic field. *Journal of Geophysical Research*, *79*(28), 4186–4194. https://doi.org/10.1029/JA079i028p04186

Huang, S. Y., Zhou, M., Sahraoui, F., Vaivads, A., Deng, X. H., André, M., et al. (2012). Observations of turbulence within reconnection jet in the presence of guide field. *Geophysical Research Letters*, *39*(11), L11104. https://doi.org/10.1029/2012GL052210

Keiling, A. (2008). Alfvén waves and their roles in the dynamics of the Earth's magnetotail: A review. *Space Science Reviews*, *142*(1–4), 73–156. https://doi.org/10.1007/s11214-008-9463-8

Kepko, L., McPherron, R. L., Amm, O., Apatenkov, S., Baumjohann, W., Birn, J., et al. (2015). Substorm Current wedge revisited. *Space Science Reviews*, *190*(1–4), 1–46. https://doi.org/10.1007/s11214-014-0124-9

Kozak, L. V., Petrenko, B. A., Lui, A. T. Y., Kronberg, E. A., & Daly, P. W. (2021). Processes in the current disruption region: From turbulence to dispersion relation. *Journal of Geophysical Research: Space Physics*, *126*(1), e2020JA028404. https://doi.org/10.1029/2020JA028404

Lockwood, M., & Cowley. (2022). Magnetosphere-ionosphere coupling: Implications of non-equilibrium conditions. *Front. Astron. Space Sci.*, *9*, 908571. https://doi.org/10.3389/fspas.2022.908571

Lui, A. T. Y., Chang, C.-L., Mankofsky, A., Wong, H.-K., & Winske, D. (1991). A cross-field current instability for substorm expansions. *Journal of Geophysical Research*, *96*(A7), 11389–11401. https://doi.org/10.1029/91JA00892

Ma, Z. W., Wang, X. G., & Bhattacharjee, A. (1995). Growth, sudden enhancement, and relaxation of current sheets in the magnetotail: Two-dimensional substorm dynamics. *Geophysical Research Letters*, *22*(21), 2985–2988. https://doi.org/10.1029/95GL02937

Milan, S. E., Clausen, L. B. N., Coxon, J. C., Carter, J. A., Walach, M. T., Laundal, K., et al. (2017). Overview of solar wind–magnetosphere–ionosphere–atmosphere coupling and the generation of magnetospheric currents. *Space Science Reviews*, *206*(1–4), 547–573. https://doi.org/10.1007/s11214-017-0333-0

Nakamura, R., Baumjohann, W., Asano, Y., Runov, A., Balogh, A., Owen, C. J., et al. (2006). Dynamics of thin current sheets associated with magnetotail reconnection. *Journal of Geophysical Research*, *111*(A11), A11206. https://doi.org/10.1029/2006JA011706

Neagu, E., Borovsky, J. E., Gary, S. P., Jorgensen, A. M., Baumjohann, W., & Treumann, R. A. (2005). Statistical survey of magnetic and velocity fluctuations in the near-Earth plasma sheet: International Sun Earth Explorer (ISEE-2) measurements. *Journal of Geophysical Research*, *110*(A5), A05203. https://doi.org/10.1029/2004JA010448

Neagu, E., Borovsky, J. E., Thomsen, M. F., Gary, S. P., Baumjohann, W., & Treumann, R. A. (2002). Statistical survey of magnetic field and ion velocity fluctuations in the near-Earth plasma sheet: Active Magnetospheric Particle Trace Explorers/Ion Release Module (AMPTE/IRM) measurements. *Journal of Geophysical Research*, *107*(A7). https://doi.org/10.1029/2001JA000318

Nguyen, H., Aunai, N., Michotte de Welle, B., Jeandet, A., Lavraud, B., & Fontaine, D. (2022). An advanced gradient boosting classifier for plasma region classification and boundary identification. *Journal of Geophysical Research: Space Physics*, *127*(1), e2021JA029773. https://doi.org/10.1029/2021JA029773

Osman, K., Kiyani, K. H., Matthaeus, W. H., Hnat, B., Chapman, S. C., & Khotyaintsev, Y. V. (2015). Multi-spacecraft measurement of turbulence within a magnetic reconnection jet. *The Astrophysical Journal Letters*, *815*(2), L24. https://doi.org/10.1088/2041-8205/815/2/L24

Oughton, S., Matthaeus, W. H., Wan, M., & Osman, K. T. (2015). Anisotropy in solar wind plasma turbulence. *Philosophical Transactions of the Royal Society A: Mathematical, Physical and Engineering Sciences*, *373*(2041), 20140152. https://doi.org/10.1098/rsta.2014.0152

Palmroth, M., Pulkkinen, T. I., Ganse, U., Pfau-Kempf, Y., Koskela, T., Zaitsev, I., et al. (2023). Magnetotail plasma eruptions driven by magnetic reconnection and kinetic instabilities. *Nature Geoscience*, *16*(7), 570–576. https://doi.org/10.1038/s41561-023-01206-2

Parker, E. N. (1958). Dynamics of the interplanetary gas and magnetic fields. *ApJ*, *128*, 664. https://doi.org/10.1086/146579

Petrukovich, A. A., Baumjohann, W., Nakamura, R., Mukai, T., & Troshichev, O. A. (2000). Small substorms: Solar wind input and magnetotail dynamics. *Journal of Geophysical Research*, *105*(A9), 21–109. https://doi.org/10.1029/2000JA900057

Pollock, C., Moore, T., Jacques, A., Burch, J., Gliese, U., Saito, Y., et al. (2016). Fast plasma investigation for magnetospheric multiscale. *Space Science Reviews*, *199*(1–4), 331–406. https://doi.org/10.1007/s11214-016-0245-4

Quinlan, J. R. (1986). Induction of decision trees. *Machine Learning*, *1*(1), 81–106. https://doi.org/10.1007/BF00116251

Russell, C. T., Anderson, B. J., Baumjohann, W., Bromund, K. R., Dearborn, D., Fischer, D., et al. (2016). The magnetospheric multiscale magnetometers. *Space Science Reviews*, *199*(1–4), 189–256. https://doi.org/10.1007/s11214-014-0057-3

Šafránková, J., Němeček, Z., Němec, F., Montagud-Camps, V., Verscharen, D., Verdini, A., & Ďurovcová, T. (2021). Anisotropy of magnetic field and velocity fluctuations in the solar wind. *The Astrophysical Journal*, *913*(1), 80. https://doi.org/10.3847/1538-4357/abf6c9

Sato, T., & Hasegawa, A. (1982). Externally driven magnetic reconnection versus tearing mode instability. *Geophysical Research Letters*, *9*(1), 52–55. https://doi.org/10.1029/GL009i001p00052

Schindler, K., & Birn, J. (1982). Self-consistent theory of time-dependent convection in the Earth's magnetotail. *Journal of Geophysical Research*, *87*(A4), 2263–2275. https://doi.org/10.1029/JA087iA04p02263

Serianni, G., Agostini, M., Antoni, V., Cavazzana, R., Martines, E., Sattin, F., et al. (2007). Coherent structures and transport properties in magnetized plasmas. *Plasma Physics and Controlled Fusion*, *49*(12B), B267–B280. https://doi.org/10.1088/0741-3335/49/12b/s25

Sokolova, M., & Lapalme, G. (2009). A systematic analysis of performance measures for classification tasks. *Information Processing & Management*, *45*(4), 427–437. https://doi.org/10.1016/j.ipm.2009.03.002

Strangeway, McFadden, J. P., Bonnell, J. W., Carlson, C. W., Ergun, R. E., & Strangeway, R. J. (2008). The turbulent Alfvénic aurora. *Physical Review Letters*, *100*(17), 175003. https://doi.org/10.1103/PhysRevLett.100.175003

Tian, A. M., Zong, Q. G., Wang, Y. F., Shi, Q. Q., Fu, S. Y., & Pu, Z. Y. (2010). A series of plasma flow vortices in the tail plasma sheet associated with solar wind pressure enhancement. *Journal of Geophysical Research*, *115*(A9), A09204. https://doi.org/10.1029/2009JA014989

Tu, C.-Y., & Marsch, E. (1993). A model of solar wind fluctuations with two components: Alfvén waves and convective structures. *Journal of Geophysical Research*, *98*(A2), 1257–1276. https://doi.org/10.1029/92JA01947

Ukhorskiy, A. Y., Sorathia, K. A., Merkin, V. G., Crabtree, C., Fletcher, A. C., Malaspina, D. M., & Schwartz, S. J. (2022). Cross-scale energy cascade powered by magnetospheric convection. *Scientific Reports*, *12*(1), 4446. https://doi.org/10.1038/s41598-022-08038-x

Verscharen, D., Klein, K. G., & Maruca, B. A. (2019). The multi-scale nature of the solar wind. *Living Reviews in Solar Physics*, *16*(1), 5. https://doi.org/10.1007/s41116-019-0021-0

Volwerk, M., Baumjohann, W., Glassmeier, K. H., Nakamura, R., Zhang, T. L., Runov, A., et al. (2004). Compressional waves in the Earth's neutral sheet. *Annals of Geophysics*, *22*(1), 303–315. https://doi.org/10.5194/angeo-22-303-2004

Vörös, Z., Baumjohann, W., Nakamura, R., Runov, A., Volwerk, M., Balogh, A., & Rème, H. (2005). Scale-dependent anisotropy of magnetic fluctuations in the Earth's plasma sheet. In *Multiscale coupling of sun-earth processes* (pp. 29–38). Elsevier. https://doi.org/10.1016/B978-044451881-1/50003-4

Vörös, Z., Baumjohann, W., Nakamura, R., Volwerk, M., Runov, A., Zhang, T. L., et al. (2004). Magnetic turbulence in the plasma sheet. *Journal of Geophysical Research*, *109*, A11215. https://doi.org/10.1029/2004JA010404

Wang, C., Han, J. P., Li, H., Peng, Z., & Richardson, J. D. (2014). Solar wind-magnetosphere energy coupling function fitting: Results from a global MHD simulation. *Journal of Geophysical Research: Space Physics*, *119*(8), 6199–6212. https://doi.org/10.1002/2014JA019834

Wang, J., Liu, X., Dai, F., Zheng, R., Han, Y., Wang, Y., et al. (2025). Automated plasma region classification and boundary layer identification using machine learning. *Remote Sensing*, *17*(9), 1565. https://doi.org/10.3390/rs17091565

Wang, T., Cao, J., Fu, H., Meng, X., & Dunlop, M. (2016). Compressible turbulence with slow-mode waves observed in the bursty bulk flow of plasma sheet. *Geophysical Research Letters*, *43*(5), 1854–1861. https://doi.org/10.1002/2016GL068147

Weygand, J. M., Kivelson, M. G., Khurana, K. K., Schwarzl, H. K., Thompson, S. M., McPherron, R. L., et al. (2005). Plasma sheet turbulence observed by cluster II. *Journal of Geophysical Research*, *110*(A1), A01205. https://doi.org/10.1029/2004JA010581

Weygand, J. M., Kivelson, M. G., Khurana, K. K., Schwarzl, H. K., Walker, R. J., Balogh, A., et al. (2006). Non-self-similar scaling of plasma sheet and solar wind probability distribution functions of magnetic field fluctuations. *Journal of Geophysical Research*, *111*(A11), A11209. https://doi.org/10.1029/2006JA011820

Weygand, J. M., Matthaeus, W. H., Dasso, S., & Kivelson, M. G. (2011). Correlation and taylor scale variability in the interplanetary magnetic field fluctuations as a function of solar wind speed. *Journal of Geophysical Research*, *116*(A8), A08102. https://doi.org/10.1029/2011JA016621

Weygand, J. M., Matthaeus, W. H., Dasso, S., Kivelson, M. G., Kistler, L. M., & Mouikis, C. (2009). Anisotropy of the taylor scale and the correlation scale in plasma sheet and solar wind magnetic field fluctuations. *Journal of Geophysical Research*, *114*(A7), A07213. https://doi.org/10.1029/2008JA013766

Zhang, L. Q., Baumjohann, W., Dai, L., Khotyaintsev, Y. V., & Wang, C. (2019). Measurements of the vorticity in the bursty bulk flows. *Geophysical Research Letters*, *46*(17–18), 10322–10329. https://doi.org/10.1029/2019GL084597

Zhang, L. Q., Baumjohann, W., Khotyaintsev, Y. V., Burch, J. L., Webster, J., Wang, J. Y., et al. (2020). BBF deceleration down-tail of $X < -15$ RE from MMS observation. *Journal of Geophysical Research: Space Physics*, *125*(2), e2019JA026837. https://doi.org/10.1029/2019JA026837

Zhang, L. Q., Baumjohann, W., Wang, J. Y., Rème, H., Dunlop, M. W., & Chen, T. (2015). Statistical characteristics of slow earthward and tailward flows in the plasma sheet. *Journal of Geophysical Research: Space Physics*, *120*(8), 6199–6206. https://doi.org/10.1002/2015JA021354

Zhang, L. Q., Dai, L., Baumjohann, W., Lui, A. T. Y., Wang, C., Rème, H., & Dunlop, M. W. (2016). Temporal evolutions of the solar wind condition at 1 AU prior to the near-earth X-lines in the tail: Superposed epoch analysis. *Journal of Geophysical Research*, *121*(8), 7488–7496. https://doi.org/10.1002/2016ja022687

Zhang, L. Q., Dai, L., Baumjohann, W., Rème, H., Dunlop, M. W., & Wei, X. H. (2015). Parallel-dominant and perpendicular-dominant components of the fast bulk flows: Comparing with the PSBL beams. *Journal of Geophysical Research: Space Physics*, *120*(11), 9500–9512. https://doi.org/10.1002/2015JA021669

Zhang, L. Q., Lui, A. T. Y., Baumjohann, W., Wang, C., Burch, J. L., & Khotyaintsev, Y. V. (2020). Anisotropic vorticity within bursty bulk flow turbulence. *Journal of Geophysical Research: Space Physics*, *125*(10), e2020JA028255. https://doi.org/10.1029/2020JA028255

Zhang, L. Q., Wang, C., Baumjohann, W., Wang, R. S., Wang, J. Y., Burch, J. L., & Khotyaintsev, Y. V. (2023). First observation of fluid-like eddy-dominant bursty bulk flow turbulence in the Earth's tail plasma sheet. *Scientific Reports*, *13*(1), 19201. https://doi.org/10.1038/s41598-023-45867-w

Zhang, L. Q., Wang, C., Dai, L., Baumjohann, W., Lui, A. T. Y., Burch, J. L., et al. (2022). Vorticity within bursty bulk flows: Convective versus kinetic. *Journal of Geophysical Research: Space Physics*, *127*(3), e2020JA028934. https://doi.org/10.1029/2020JA028934

Zhang, L. Q., Wang, C., Dai, L., Ren, Y., & Lui, A. T. (2022). A statistical study on wide-amplitude kinetic Alfvénic pulse at 8–12R_E in the magnetotail by THEMIS spacecraft from 2008 to 2010. *Journal of Geophysical Research: Space Physics*, *127*(2), e2021JA029593. https://doi.org/10.1029/2021JA029593

Zhang, L. Q., Wang, J. Y., Baumjohann, W., Rème, H., & Dunlop, M. W. (2015). Earthward and tailward flows in the plasma sheet. *Journal of Geophysical Research: Space Physics*, *120*(6), 4487–4495. https://doi.org/10.1002/2015JA021154

Zhao, L.-L., Zank, G. P., & He, J. S. (2022). Observations of waves and structures by frequency-wavenumber spectrum in solar wind turbulence. *The Astrophysical Journal*, *944*(2), 98. https://doi.org/10.3847/1538-4357/acb33b

Zimbardo, G., Greco, A., Sorriso-Valvo, L., Perri, S., Vörös, Z., Aburjania, G., et al. (2010). Magnetic turbulence in the geospace environment. *Space Science Reviews*, *156*(1–4), 89–134. https://doi.org/10.1007/s11214-010-9692-5